FULL PAPER

2D Materials

ADVANCED
FUNCTIONAL
MATERIALS

www.afm-journal.de

A Multibeam Interference Model for Analyzing Complex Near-Field Images of Polaritons in 2D van der Waals Microstructures

Baoxin Liao, Xiangdong Guo, Debo Hu, Feng Zhai, Hai Hu, Ke Chen, Chen Luo, Mengkun Liu, Xiaoxia Yang,* and Qing Dai*

Van der Waals (vdW) materials are among the most promising candidates for photonic integrated circuits because they support a full set of polaritons that can manipulate light at deep subdiffraction nanoscale. It is possible to directly probe the propagating polaritons in vdW materials in real space via scattering-type scanning near-field optical microscopy, such that the wave vector and lifetime of the polaritons can be extracted from as-measured interference fringes by Fourier analysis. However, this method is unsuitable for clutter interference patterns in samples exhibiting inadequate fringes due to small size (less than 10 μm) or complex edges that are often encountered in nanophotonic devices and new material characterization. Here, a multibeam interference model is developed to analyze complex images by disentangling them into periodic patterns and residue. By employing phase stationary approximation, polariton wave vector can be derived from offset ratio of the center point, and the ratio of polariton reflection and scattering rates at the edge is obtained from the ratio of the periodic and aperiodic patterns. This method can be widely used in the optical characterization of new vdW materials that are difficult to synthesize into large crystals, as well as nanophotonic integrated devices with unique boundaries.

B. X. Liao, X. D. Guo, Dr. D. B. Hu, Dr. H. Hu, K. Chen, C. Luo,
Prof. X. X. Yang, Prof. Q. Dai
Division of Nanophotonics
CAS Center for Excellence in Nanoscience
National Center for Nanoscience and Technology
Beijing 100190, P. R. China
E-mail: yangxx@nanoctr.cn; daiq@nanoctr.cn
B. X. Liao, X. D. Guo, Dr. D. B. Hu, Dr. H. Hu, K. Chen, C. Luo,
Prof. X. X. Yang, Prof. Q. Dai
Center of Materials Science and Optoelectronics Engineering
University of Chinese Academy of Sciences
Beijing 100049, P. R. China
Prof. F. Zhai
Department of Physics
Zhejiang Normal University
Jinhua 321004, P. R. China
Prof. M. K. Liu
Department of Physics and Astronomy
Stony Brook University
Stony Brook, NY 11794, USA

The ORCID identification number(s) for the author(s) of this article can be found under https://doi.org/10.1002/adfm.201904662.

1. Introduction

The emergence of graphene and other 2D van der Waals (vdW) materials has sparked interest in a newly discovered phenomenon: highly confined polaritons that can break the diffraction limit and confine light into the deep subdiffraction nanoscale.[1,2] 2D vdW materials comprise a large family of matter that can support a full set of complementary polaritons. This trait imparts versatile properties that may be suitable for future nanophotonic devices.[3–6] Some examples of such properties include the dynamic tunability via gating of plasmons in graphene and black phosphorus,[7–10] the long lifetimes of hyperbolic phonon polaritons (HPs) in dielectric hexagonal boron nitride (h-BN) and MoO_3 crystals,[11–13] and the strong light–matter interaction of exciton polaritons in semiconducting $MoSe_2$ and WSe_2 crystals.[14,15]

The development of vdW polaritons largely depends on the progress of scattering-type scanning near-field optical microscopy (s-SNOM) with ultrahigh spatial resolution (about 15 nm, defined by the microscope's tip).[16,17] Graphene plasmon propagation was first experimentally resolved in real space via s-SNOM,[7] which prompted studies probing the propagation of many other vdW polaritons.[10,11,13,14,16] The results of these s-SNOM nanoimaging studies have unveiled numerous extraordinary properties of vdW polaritons. For example, high-quality graphene encapsulated between two h-BN films possesses plasmons that exhibit unprecedentedly low damping combined with strong field confinement,[18] HPs in h-BN can be controlled by crystal thickness,[11] HPs in MoO_3 crystals display in-plane anisotropy with high confinement and low loss,[13] and the propagating direction of HPs can be controlled by metasurfaces.[19] Numerous studies have demonstrated applications of s-SNOM nanoimaged vdW polaritons, including hot electron detection,[20–22] surface-enhanced infrared (IR) absorption,[23] ultrafast plasmonic switching,[17] observation of slow light,[24] metasurface engineering,[19] hyperfocusing lens,[25,26] and probing optical constants.[27]

The s-SNOM nanoimaging is performed by recording interference fringes formed by polaritons that are excited, reflected, and scattered by the s-SNOM tip and sample edges. The polaritons'

**ADVANCED
SCIENCE NEWS**
www.advancedsciencenews.com

*ADVANCED
FUNCTIONAL
MATERIALS*
www.afm-journal.de

wavelengths and lifetimes are extracted from Fourier analysis of the interference fringes.[12,14] To meet the standards for Fourier analysis, only interference fringes that either contain many cycles (>10) or are formed by the interference of only two light beams are considered in previous works. For example, a typical s-SNOM image of graphene plasmons or h-BN HPs contains uniformly distributed interference fringes parallel to the edges, with the interfringe distance equal to half of the polariton wavelength. These fringes result from the interference of the incident light and tip-launched polaritons that are propagating and reflected by the edge.[18,28] It is valid to ignore the scattering and excitation of polaritons at the edges due to the vdW polaritons' large wave vectors. Another typical s-SNOM image of graphene plasmon or h-BN HP systems incorporating gold nanoantennas demonstrates a fringe distance equal to the plasmon wavelength.[29–31] In this case, the fringes are formed by the interference of the incident light and the antenna-launched polaritons propagating to the s-SNOM tip, while the tip-launched polaritons that are reflected by the edge are damped out in the region sufficiently far from the gold edge. A third typical s-SNOM image is obtained by mapping a MoS_2 waveguide, where interference between the tip-launched and edge-scattering signal and the tip-scattering signal forms fringes, and the edge reflection and excitation may be ignored if the sample is large and transparent.[27]

However, the analysis of irregular s-SNOM images in samples exhibiting small sizes or complex edges has remained elusive since Fourier analysis is invalid when there are limited fringes or complex signals, as occurs near edges. In these samples, it is important to take into account polaritons that are excited, scattered, and reflected by both the microscope tip and the sample edges, which vary according to the working frequency, the presence of edges, and sample size. However, in addition to the invalidation of Fourier analysis, the widely used numerical method is also unsuitable to this problem because it cannot simulate multibeam interference (MBI) due to its inability to consider edge-scattered signals. Therefore, it is essential to identify a model that can consider multiple beams and reconstruct irregular near-field images.

In this work, we develop an MBI model to analyze irregular s-SNOM fringes in samples exhibiting small size or complex boundaries. Using the model, we reconstruct a series of irregular interference fringes of imaged HPs in h-BN microdisks, wherein we vary the boundary or the excitation frequency. From mathematic analysis, s-SNOM images can be disentangled into periodic patterns and residue for separate resolution. By introducing the phase stationary approximation to solve the aperiodic interference pattern, we can calculate the in-plane wave vector from the offset distance of the center point. Polariton reflection and scattering at the sample edge, which are important for functional devices, can also be extracted and studied for their relation to the boundary media and working frequency. This demonstrated method may be useful for novel material characterization and nanophotonic device design.

2. Results and Discussion

We select HPs in h-BN microdisks to serve as an example for illustrating the MBI model. **Figure 1**a schematically shows the four main pathways of light involved in the s-SNOM measurement,

which are designated U_1 through U_4.[8,14,30] U_1 depicts the portion of incident light that is directly scattered back by the tip (tip-reflected). U_2 depicts the tip-launched phonon polaritons that propagate outward from the tip as circular waves before they are scattered into free space by the sample's edge (tip-launched/edge-scattered). U_3 represents the tip-launched phonon polaritons that propagate outward to the edge and are then reflected back before they are scattered by the tip into the detector (tip-launched/edge-reflected/tip-scattered). U_4 depicts the edge-launched polaritons that are scattered into detector by the tip (edge-launched/tip-scattered). We note that light scattered directly by the edge (designated U_5) may also be collected, but it needs not be considered separately. Since the interference fringes of U_5 and U_1 are determined by the free space wavelength of light, their space is comparable to the disk size and they can be neglected and considered as background for the polaritons. The interference patterns between U_5 and U_2/U_4 are similar to those of U_1 and U_2. The interference pattern between U_5 and U_3 exhibits different near-field features that are not observed in our experiment (see Section I in the Supporting Information). Scattered light after multiple reflections is neglected due to large multiplicative losses.

Near-field images map the signal strength. As an example, we calculate the sum of U_1, U_2, U_3, and U_4 signals at an arbitrary point S in a disk (Figure 1a). The x–y plane is set as the sample surface. The laser beam illuminates the tip–sample system along the direction $\vec{e}_{in} = (\cos \alpha, 0, -\sin \alpha)$, where α is the angle between the incident beam and the x–y plane. For an arbitrary point P on the sample edge, R is the tip–edge distance $|SP|$ and θ is the angle of $\overrightarrow{SP}$ relative to positive direction of the x-axis. Therefore, the signals for U_1 through U_4 can be written as

$$U_j = A_j \, e^{i\phi_j}, \quad j = 1, 2, 3, 4 \tag{1}$$

where A_j is the amplitude and ϕ_j is the phase. We set $\phi_1 = 0$. The phase delays of U_2 and U_4 are $\phi_2 = \phi_4 = k_\perp R \cos\theta + Rq$, where $k = k_0 \cos \alpha$, $k_0 = 2\pi/\lambda_0$ is the free-space wave vector, and q is the in-plane wave vector of the HPs. The phase delay between U_3 and U_1 is $\phi_3 = 2qR$, as the HPs travel a distance of $2R$. The amplitudes are related to the scattering rate, reflectivity, excitation factor of HPs at the sample's edges and the s-SNOM tip, and the HPs' decay. Due to the reciprocity theorem,[32,33] the scattering and excitation of HPs are reversible processes. We designate the scattering and excitation rates at the tip and the edge as η_t and η_e, respectively. The decay of the HPs away from the tip results from electrical impurity or crystal defect–induced damping ($\approx e^{-R/a}$, where a is the decay length)[34,35] and circular-wave geometrical spreading stemming from energy conservation ($\approx R^{-1/2}$). We can therefore specify $A_1 = \eta_s A_0$, $A_2 = \eta_t \eta_e A_0 R^{-1/2} e^{-R/a}$, $A_3 = \eta_t^2 \eta_R A_0 (2R)^{-1/2} e^{-2R/a}$, and $A_4 = \eta_e \eta_t A_0 R^{-1/2} e^{-R/a}$, where A_0 is the amplitude of the incident laser beam, η_s is the scattering rate of incident light back into the detector, and η_R is the reflectivity of HPs at the edge. The total optical signal $|U|$ can be defined as

$$|U| = \left| \sum_{j=1,2,3,4} U_j \right| = \left| U_1 + \sum_{j=2,3,4} \int_0^{2\pi} U_j R \, d\theta \right|$$

$$= \left| \eta_t A_0 \left(\frac{\eta_s}{\eta_t} + 2\eta_e \int_0^{2\pi} \sqrt{R} \, e^{-R/a} \, e^{i(k_\perp \cos\theta + q)R} \, d\theta + \eta_t \eta_R \int_0^{2\pi} \sqrt{2R} \, e^{-2R/a} \, e^{i2qR} \, d\theta \right) \right| \tag{2}$$
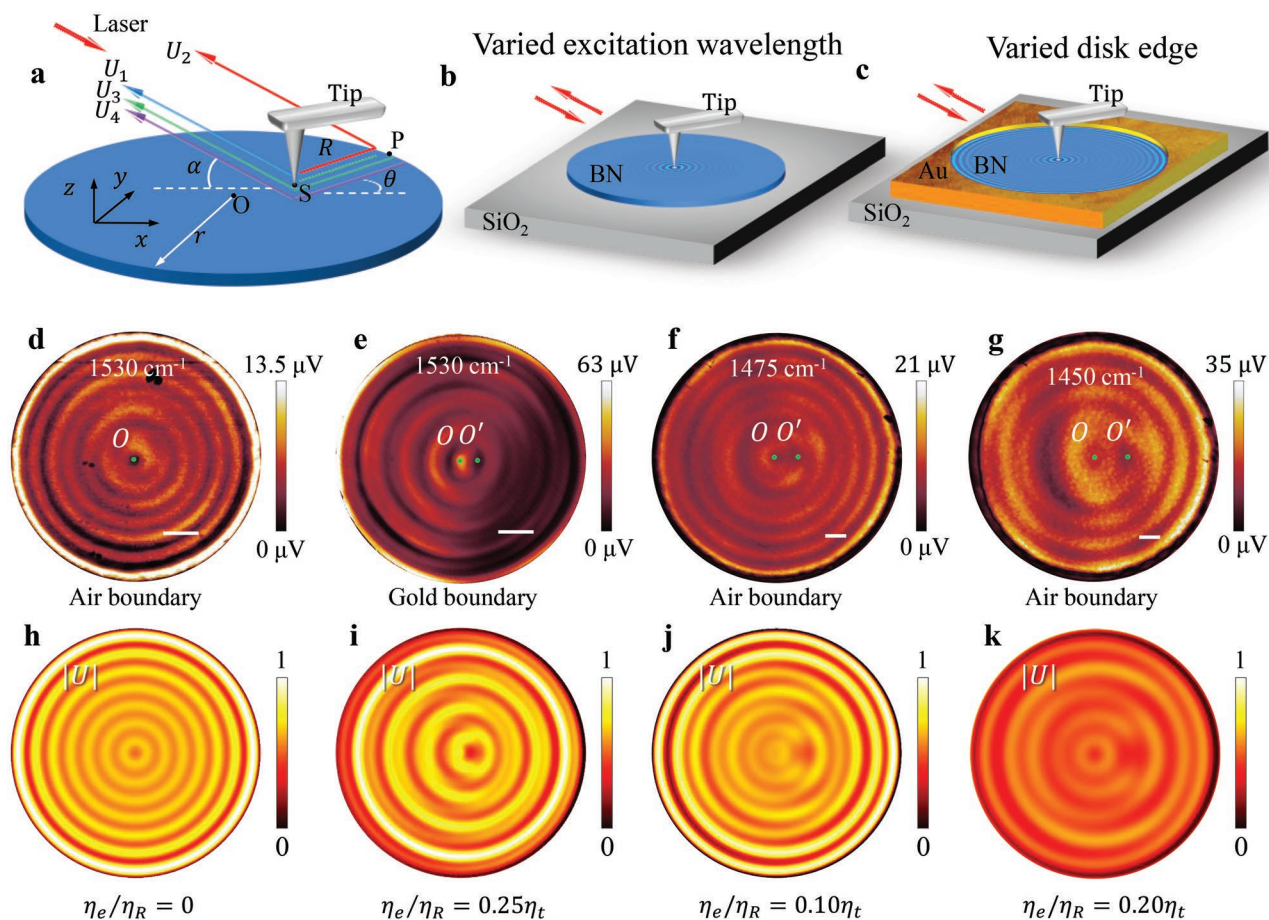
Figure 1. The multibeam near-field imaging of HPs in h-BN disks. a) Schematic of s-SNOM imaging with incident laser and the main four back-scattered optical beams (U_1–U_4), which could be collected by the photodetector. O is the geometrical center. S and P are arbitrary points in the disk and at the edge, respectively. b,c) Schematic of nanoimaging of h-BN disks with air and gold boundaries, respectively. d–g) Near-field images of HPs in h-BN disks with varied frequencies and boundaries, as indicated in the images. Their thickness are d) 140 nm, e) 114 nm, and f,g) 125 nm, respectively. Scale bar: 1 µm. The disk radii are d,e) 3.5 µm and f,g) 6 µm. h–k) The calculated near-field images $|U|$ with $\eta_e/\eta_R = 0$, $0.25\eta_t$, $0.10\eta_t$, and $0.20\eta_t$, respectively.

The phase delay of the third term in Equation (2) scales only with tip–edge distance R, which contributes uniform interference fringes. The phase delay of the second term is strongly dependent on the incident/back-scattered angle α ($\alpha = \pi/6$ in our experimental facility), which is key to the irregular interference patterns. The ratio of these two terms depends on η_t, η_R, and η_e, which are determined by the working frequency and edge properties, among other factors.

We measured HPs in h-BN microdisks as a function of varied sample edges and excitation wavelengths (details provided in the Experimental Section). Figure 1b,c schematically demonstrate that the h-BN microdisks are subject to global illumination via an IR laser beam, such that both the tip and edge excitation and scattering exist. Scanning the microdisks with the microscope tip allows for visualization of the interference fringes. Figure 1d,e depict the near-field images of HPs in h-BN disks with boundaries comprised of air and gold, respectively, at 1530 cm^{-1}. Uniformly distributed fringes characterized by a stable period are observed in the h-BN disk with an air boundary (Figure 1d), while the near-field image of the h-BN disk with a gold boundary (Figure 1e) exhibits three distinct features. First, there is no

stable period between the interference fringes, as the period in the left-hand region of the microdisk is larger than that of the right-hand region. Second, the center of the circles (O') is located to the right of the disk center (O). Third, the interference fringes' behavior resembles that of a wave packet (i.e., two bright fringes form a period). The near-field images of HPs in the h-BN disk with an air boundary are measured at new excitation wavelengths, i.e., 1475 and 1450 cm^{-1}, which also exhibit distinct features, as shown in Figure 1f,g. The 1475 cm^{-1} excitation prompts deformation of the second fringe, as well as the appearance of a dark spot, designated O', to the right of the center point. The quantity $|OO'|$ increases as the excitation frequency decreases from 1475 to 1450 cm^{-1}. These features imply that the image in Figure 1d mainly contains the periodic pattern, while the other three images in Figure 1e–g are the superposition of periodic and aperiodic patterns.

The polariton wave vector is extracted from the s-SNOM images according to Equation (2). When periodic traits are dominant, an s-SNOM image can be fitted by a periodic image with similar features (such as the number and distribution of fringes). For example, Figure 1d–g can be simulated by using

ADVANCED
SCIENCE NEWS
www.advancedsciencenews.com

ADVANCED
FUNCTIONAL
MATERIALS
www.afm-journal.de

$q = 7.15k_{0,X}$, $8.2k_{0,X}$, $4.1k_{0,X}$, and $3.1k_{0,X}$, where $X = 1530$, 1530, 1475, and 1450 cm^{-1}, respectively (see Section II in the Supporting Information). For all of the HPs, the decay length a is set to $10\pi/q$. When an s-SNOM image possesses dominant aperiodic traits, q can be extracted from the location of O' using the second term in Equation (2) according to the following procedure.

We introduce the method of stationary phase to obtain an approximate analytical solution of the second term in Equation (2),[36] since this term is a transcendental integral that cannot be calculated directly. The theoretical derivation is as follows. Point $S(x_0,y_0)$ inside the disk satisfies the geometric constraint

$$(x_0 + R\cos\theta)^2 + (y_0 + R\sin\theta)^2 = r^2 \qquad (3)$$

A direct calculation gives

$$\frac{dR}{d\theta} = \frac{R(x_0\sin\theta - y_0\cos\theta)}{x_0\cos\theta + y_0\sin\theta + R} \qquad (4)$$

The phase $\phi = (k_\perp\cos\theta + q)R$ is stationary when

$$\frac{d\Phi}{d\theta} = -k_\perp R\sin\theta + (k_\perp\cos\theta + q)\frac{dR}{d\theta} = 0 \qquad (5)$$

Combining with Equations (4) and (5) yields

$$(qx_0 - k_\perp R)\sin\theta = y_0(k_\perp + q\cos\theta) \qquad (6)$$

According to definition of coordinates, the horizontal diameter includes $y_0 = 0$, so Equation (6) becomes $(qx_0 - k_\perp R)\sin\theta = 0$. Thus, $\theta = 0$ and $\theta = \pi$ are two stationary points. Therefore, at these points most of the light beams cancel each other due to symmetrical geometry. Furthermore, only light beams along the horizontal diameter contribute to the interference fringes.

The second derivative of ϕ is

$$\frac{d^2\Phi}{d\theta^2} = \frac{(qx_0 - k_\perp R)R\cos\theta}{x_0\cos\theta + R} \qquad (7)$$

which vanishes at the stationary points $\theta = 0$ when $x_0 = x_{0c} \equiv r/(q/k_\perp + 1)$ and $\theta = \pi$ when $x_0 \equiv x_{0e} = r/(q/k_\perp - 1)$. These results imply a change in the bending direction of phase at x_{0c} and x_{0e}, with the interference fringes focused at these two points. This is in good agreement with the experimental results, wherein O' appears in the s-SNOM images (Figure 1d–g). To determine whether O' is at x_0 or x_{0e}, we calculate a set of aperiodic near-field images according to the second term of Equation (2) with polariton wave vectors that vary from $q = 2k_0$ to $q = 11k_0$ in a disk of $r = 7$ μm (see details in Section III in the Supporting Information). The resulting images are presented in Figure S2 (Supporting Information), from which the $|OO'|$ values are extracted. We plot $|O'O|/r$ as a function of q (unfilled violet circles) in **Figure 2**a, where x_{0c}/r and x_{0e}/r are also plotted (solid and dotted lines, respectively). The $|O'O|/r$ data overlap with the x_{0c}/r function, indicating that the observed O' point in the near-field images is located at $x_{0c} \equiv r/(q/k_\perp + 1)$. Thus, the

calculation gives the relation between the in-plane wave vector and the offset ratio μ as follows:

$$\mu = \frac{|O'O|}{r} = \frac{x_{0c}}{r} = \frac{\cos\alpha}{q/k_0 + \cos\alpha} \qquad (8)$$

where O' is the center of aperiodic pattern and O is the geometrical center of disk. The offset ratio depends only on the polariton wave vector for a constant incident angle α, and it increases when the in-plane wave vector decreases.

Equation (8) provides a simple method to determine the wave vector through offset ratio measurement in complicated near-field images. As an example, we calculate the wave vectors of Figure 1e–g from the quantity $|OO'|/r$. When the incident light frequency decreases from 1530 to 1450 cm^{-1}, $|OO'|/r$ clearly increases from 0.095 to 0.218, while the calculated wave vector is reduced from $8.2k_0$ to $3.1k_0$. Experimental values (filled violet circles in Figure 2a) are highly consistent with theoretical predictions, providing strong support for the validity of our model and analysis. To further verify our manipulation of Equation (8), we measured waveguide modes in MoS$_2$ disks. Figure 2b shows near-field images of disks with radii of 7 to 4 μm. The aperiodic patterns, i.e., eccentric circles, are dominant in these figures due to the weak reflection of waveguide modes at the sample edge. While the small disks exhibit clutter interference fringes, the assigned location of O' is much more robust than the fringe distance measurements due to focusing of the fringes. Equation (8) estimates that the calculated wave vectors are about 2.04, 1.94, 1.84, and 1.99. These values are very close to the wave vector $q = 1.96k_0$ calculated by the finite element analysis (FEA) method for MoS$_2$/SiO$_2$/Si structure (see details in the Experimental Section), as shown in Figure 2c.

After determining the wave vector of polaritons in a given image, the aperiodic and periodic patterns are fixed. The experimental s-SNOM images can be reconstructed by optimizing the ratio $2\eta_e:\eta_t\eta_R$. The calculated near-field images that best fit the experimental images in Figure 1d–g are depicted in Figure 1h–k, wherein $\eta_e/\eta_R = 0$, $0.25\eta_t$, $0.11\eta_t$, and $0.20\eta_t$, respectively. η_t is a constant when the experimental conditions are fixed (same incident frequency, polariton, and tip parameters). These results indicate that the s-SNOM images are highly dependent on the proportion of edge scattering η_e and edge reflectivity η_R, which are affected by the boundary material and in-plane wave vector. Compared to an air boundary, the gold edge promotes more scattering and excitation while reducing the reflection of HPs. Similar phenomena are observed when the wavenumber is decreased, because better agreement with the wave vector promotes the scattering of HPs into free space.

To corroborate the above η_e/η_R findings, we perform FEA to study the reflectivity and scattering of HPs at the h-BN edges. **Figure 3**a–c shows schematic profile views of the FEA models corresponding to the sample/boundary structures in Figure 1d–f. Port 1 is set at the left end of the h-BN flake, while the boundary medium lies at the other end. The fundamental mode of the h-BN HPs (TM$_0$) is launched from port 1, from which it propagates into the h-BN before it is reflected or scattered by the edge. The reflectivity (η_R) can be defined as $\eta_R = |E_R|^2/|E_{in}|^2$, and the total scattering ratio (S) can be defined as $S = |E_S|^2/|E_{in}|^2$, where E_R and E_S are the reflected and scattered

**ADVANCED
SCIENCE NEWS**
www.advancedsciencenews.com

**ADVANCED
FUNCTIONAL
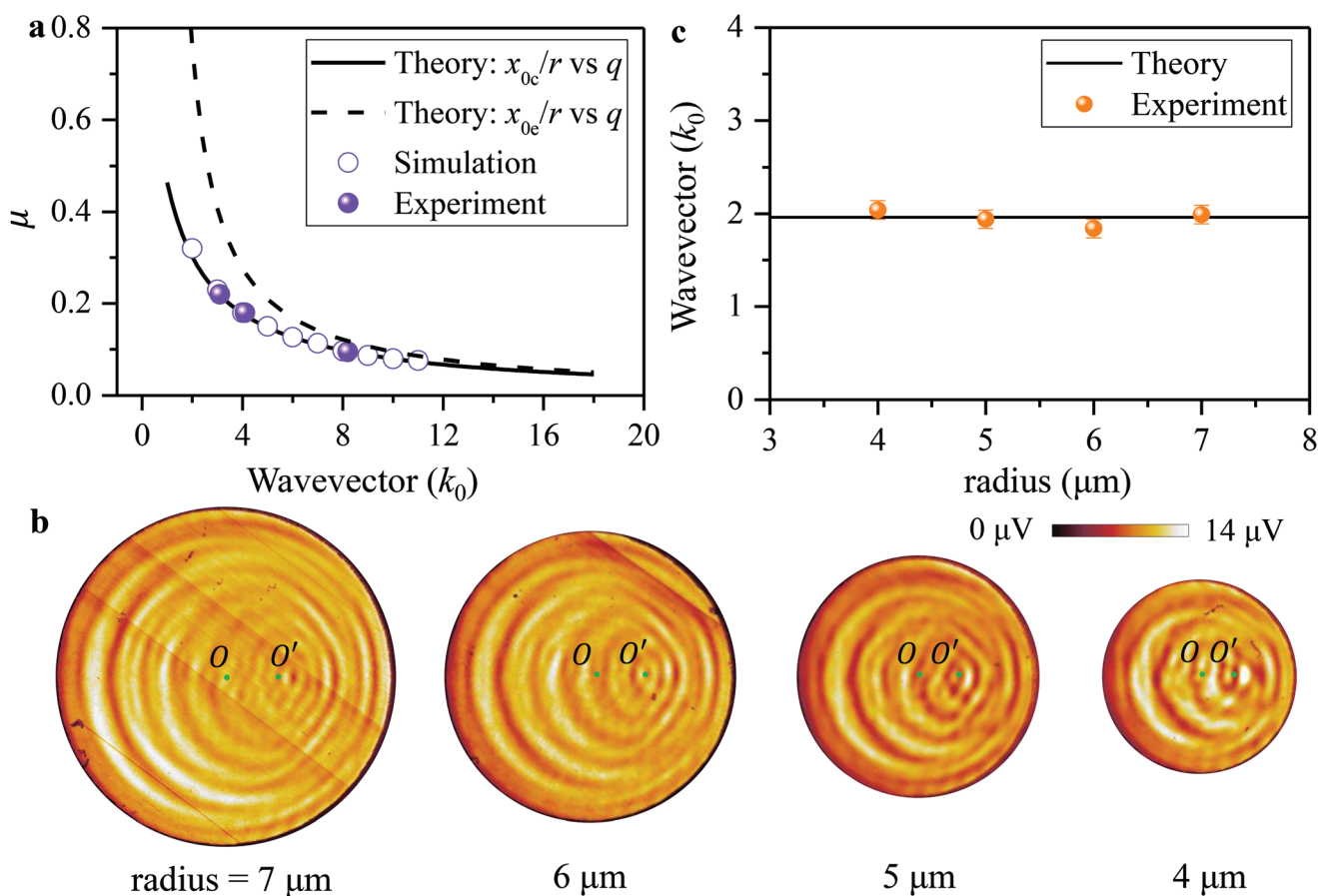MATERIALS**
www.afm-journal.de

Figure 2. Reconstruction of near-field images. a) The offset ratio $\mu = |OO'|/r$ as a function of wave vector. For convenience, we use the free-space wave vector $k_0 = 2\pi/\lambda_0$ as the unit of momentum unit. The solid line represents the theoretical calculation, while the unfilled circles represent data extracted from calculated near-field images (Figure S3, Supporting Information) and filled violet circles represent data extracted from Figure 1d–g. b) The experimental near-field images of MoS_2 disks at 1530 nm wavelength. c) The calculated wave vector of images in (b) via Equation (8), where the error bar indicates the deviation of measurement. The horizontal black line $q = 1.96k_0$ is the wave vector of 206 nm thick MoS_2 calculated by the mode analysis at 1530 nm.

energy, respectively, and E_{in} is the energy of the launched HPs. Calculations yield $\eta_R = 0.97$ and $S = 0.03$ for Figure 3a (at 1530 cm^{-1} with an air boundary), $\eta_R = 0.58$ and $S = 0.42$ for Figure 3b (at 1530 cm^{-1} with a gold boundary), and $\eta_R = 0.84$ and $S = 0.16$ for Figure 3c (at 1475 cm^{-1} with an air boundary). These values are directly related to the time-average power flow (indicated by white arrows in Figure 3a–c) of the propagating HP modes in the h-BN. Comparing Figure 3a and b, we observe that at 1530 cm^{-1} the gold boundary prompts a strong increase in the power flow scattering while the air boundary reflects nearly all of the highly confined HPs. Comparing Figure 3a,c, we note that the lower HP frequency increases the power flow scattered by the air since the HP mode is more weakly confined, as evidenced by the spatial distribution of the real part of the electrical field in the x direction E_x (Re(E_x)).

Next, we calculate S/η_R as a function of the dielectric boundary and laser frequencies, respectively. S/η_R is proportional to $2\eta_e/\eta_t\eta_R$ (the ratio of the aperiodic to the periodic patterns) and their difference comes from η_t and the relationship between the total scattering R and the partial scattering

to the detector η_e. Thus, S/η_R can be used to estimate how the s-SNOM images change with the boundary or incident frequency. Figure 3d displays S/η_R as a function of the boundary refractive index, n_{edge}. S/η_R increases from 0.03 to 1.48 as n_{edge} increases from 1 to 20, which means that the ratio of aperiodic pattern and periodic pattern increases about 50 times. Figure 3e shows S/η_R as a function of HP frequency. When the frequency decreases from 1550 to 1440 cm^{-1}, S/η_R increases from 0.02 to 0.90, corresponding to that the ratio of aperiodic pattern and periodic pattern increases 45 times. Thus, we can predict the near-field images from the polariton properties and the edges, and we can also estimate the ratio between edge scattering and edge reflection, which is meaningful in analysis of waveguide propagation and energy transmission.

At last, we can also estimate the tip efficiency with varied working frequency. From the above relations, when we denote the ratio of light scattered into the detector to the total scattering light as the constant l, we can get $\eta_e/\eta_R = 0.70l$ for Figure 1e and $\eta_e/\eta_R = 0.19l$ for Figure 1f. Combined with $\eta_e/\eta_R = 0.25\eta_t$ and $0.11\eta_t$ for Figure 1e,f as calculated earlier, the efficiency of
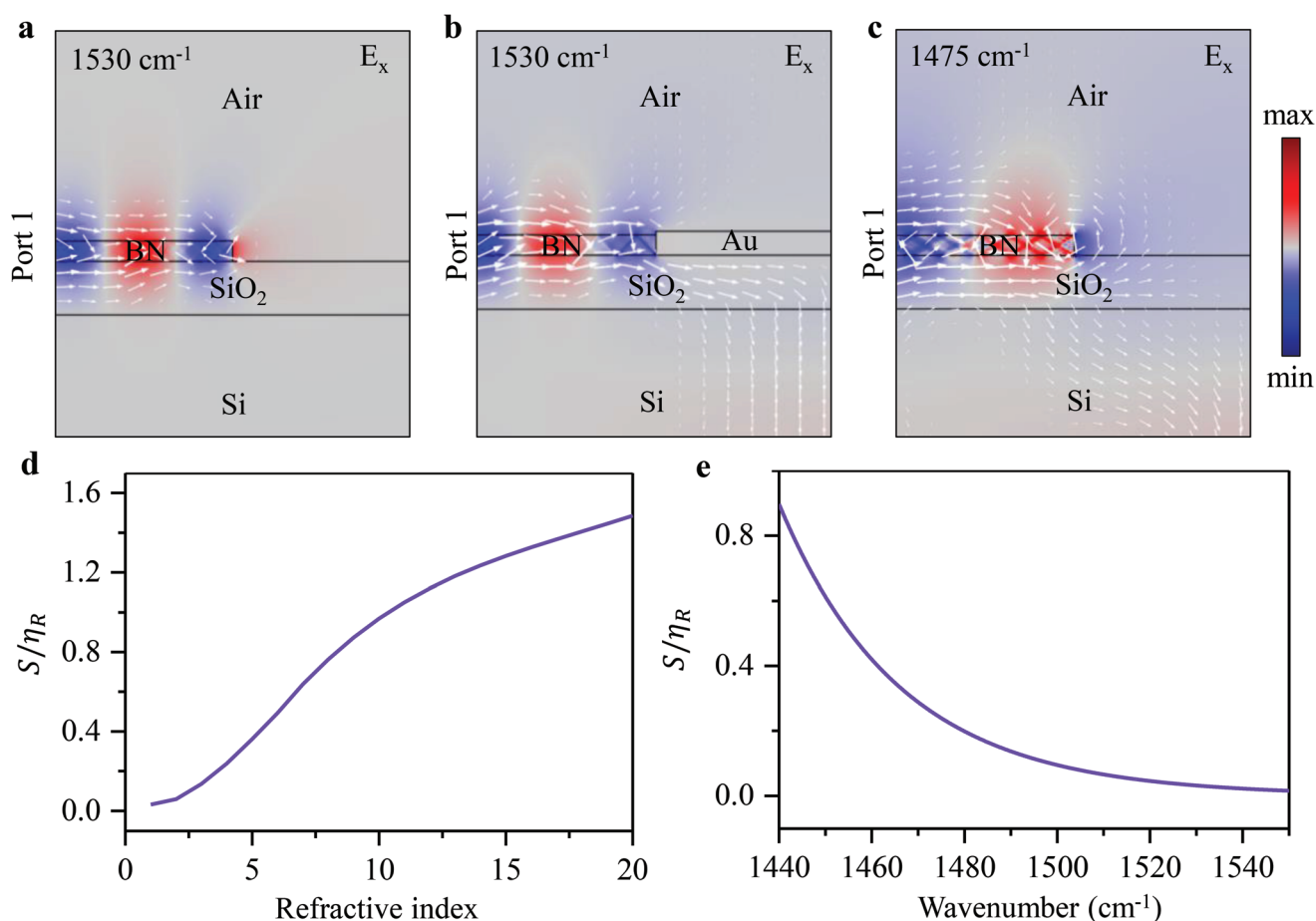
**ADVANCED
SCIENCE NEWS**
www.advancedsciencenews.com

**ADVANCED
FUNCTIONAL
MATERIALS**
www.afm-journal.de

Figure 3. Scattering and reflection of HPs at the sample edge. a–c) The schematic side views of the HPs in h-BN flake with device configuration similar to those of Figure 1d–f. The numerical calculation of the x-component of the total electric field of HPs propagating to edge is also shown. The thicknesses of h-BN, SiO$_2$, and Au are 114, 300, and 134 nm, respectively. The white arrows indicate the time-average energy flow. The calculated S/η_R as a function of d) boundary refractive index and e) working frequency, respectively.

the tip is $\eta_t = 0.70l/0.25 = 2.8l$ at 1530 cm^{-1} and $\eta_t = 0.19l/0.11 = 1.72l$ at 1475 cm^{-1}. The tip efficiency is higher at higher excitation frequencies, which agrees well with previous studies[37] since the tip acts as an antenna whose coupling efficiency increases when the wavelength is close to the tip size.

kinds of polaritons such as plasmons, phonon polaritons, and exciton polaritons, as well as waveguide modes in vdW materials. We believe that our work will be useful for characterizing more polaritons in vdW materials in the future, and that it will be meaningful for the design of functional nanophotonic devices.

3. Conclusion

In conclusion, we developed an MBI model that can reconstruct cluttered s-SNOM images. The validity of the model has been demonstrated by reconstructing experimentally observed distorted near-field images of HPs in h-BN microdisks with gold boundaries, or air boundaries imaged at relatively low frequencies. The dispersion of polaritons or waveguide modes can be derived from the displacement of the center point in the aperiodic patterns compared to the periodic patterns. The scattering rate and reflectivity of polaritons at the edge, which are important for nanophotonic devices, can also be extracted from the dielectric function of the boundary material and the working frequency. This model is applicable for various

4. Experimental Section

Sample Preparation: MoS$_2$ and h-BN microcrystals of various thicknesses were exfoliated from bulk samples on silicon wafers with a 300 nm thick SiO$_2$ top layer. Disks with air boundaries were patterned onto the sample surface using electron beam lithography (Vistec 5000bES, Germany) in poly(methyl methacrylate) followed by SF$_6$ plasma etching. Disks with gold edges were prepared by depositing and evaporating a gold film by e-beam evaporator after plasma etching.

Near-Field Optical Measurements: A commercial s-SNOM (www.neaspec.com) was used to perform near-field imaging. The s-SNOM was based on a tapping-mode AFM illuminated by monochromatic quantum cascade lasers and a Ti:Al$_2$O$_3$ laser operating in continuous-wave mode (www.toptica.com). The near-field images were extracted by a pseudo-heterodyne interferometric detection

module with a tip-tapping frequency of about 270 kHz. The tip-tapping amplitudes were 30 nm for the middle IR experiments and 50 nm for the 1530 nm wavelength experiments. The spot size of the focused middle-IR (1450–1530 cm^{-1}) beam under the AFM tip was 15–20 μm, which completely covered the h-BN disk edge. The spot size of the focused near-IR (1530 nm) beam under the AFM tip was ≈3 μm. All light from the field signal was demodulated at a frequency of 3 Ω.

Finite Element Analysis: In the simulation, the diagonal permittivity function of MoS$_2$ and h-BN are used, wherein $\varepsilon_{xx} = \varepsilon_{yy} = \varepsilon_\perp$ and $\varepsilon_{zz} = \varepsilon_\parallel$ are the components perpendicular and parallel to the anisotropy axis, respectively.[27,38] The diagonal permittivity of MoS$_2$ is $\varepsilon_{xx} = \varepsilon_{yy} = 20.25$ and $\varepsilon_{zz} = 9.61$ in the mode analysis for the MoS$_2$ waveguide modes.[27] For a wavelength of 1530 nm, the refractive indices of SiO$_2$ and Si are $n_{SiO_2} = 1.44$ and $n_{Si} = 3.47$, respectively. In the propagation analysis of b-BN HPs, the anisotropic dielectric function of h-BN is given by[39]

$$\varepsilon_m = \varepsilon_{\infty,m} + \varepsilon_{\infty,m} \frac{(\omega_{LO,m})^2 - (\omega_{TO,m})^2}{(\omega_{TO,m})^2 - \omega^2 - i\Gamma_m \omega} \tag{9}$$

where $m = \perp, \parallel$ represents in-plane and out-of-plane. The out-of-plane A$_{2u}$ phonon modes of h-BN were $\omega_{TO} = 780$ cm^{-1} and $\omega_{LO} = 830$ cm^{-1}, and the in-plane E$_{1u}$ phonon modes are $\omega_{TO} = 1370$ cm^{-1} and $\omega_{LO} = 1610$ cm^{-1}. The other parameters are $\varepsilon_{\infty,\perp} = 4.87$, $\varepsilon_{\infty,\parallel} = 2.95$, $\Gamma_\perp = 5$ cm^{-1}, and $\Gamma_\parallel = 4$ cm^{-1}. Disk thicknesses are consistent with measurements from topographic maps of the samples. The refractive indices of SiO$_2$ and Si are $n_{SiO_2} = 1.204$ and $n_{Si} = 3.42$, respectively. The refractive index of gold is $n_{Au} = 7.568$ at 1530 cm^{-1}.[40] To analyze the scattering and reflection of HPs in the sample, 2D models are designed that correspond to actual experimental structures. As shown in Figure 3a–c, two numerical ports are placed at the left and right boundaries of the simulation domain. The scattering boundary condition is applied to simulation domain's upper and lower boundaries. The fundamental mode of the HPs launched by port 1 displays a complex effective index $n + jk$. HPs could be expected to decay during propagation due to the absorption of h-BN and the substrate.[41,42] In order to obtain the energy reflection R, the scattering parameter S_{11} is recorded, and to compensate for the energy loss of the HPs, the power dissipation density (w) in h-BN and the substrate is recorded. For a 2D model, the absorption A of h-BN and the substrate can be obtained via $A = \iint_{h-BN,SiO_2,Si} w/P_{port1}$,[43,44] where P_{port1} is the power of port 1. Therefore, the energy reflection is given by $R = |S_{11}|^2 + A$. Since transmission is negligible, the total scattering is given by $S = 1 - R$.

Supporting Information

Supporting Information is available from the Wiley Online Library or from the author.

Acknowledgements

Conflict of Interest

The authors declare no conflict of interest.

[1] T. Low, A. Chaves, J. D. Caldwell, A. Kumar, N. X. Fang, P. Avouris, T. F. Heinz, F. Guinea, L. Martin-Moreno, F. Koppens, *Nat. Mater.* **2017**, *16*, 182.

[2] D. N. Basov, M. M. Fogler, F. J. García de Abajo, *Science* **2016**, *354*, aag1992.

[3] H. Hu, X. Yang, F. Zhai, D. Hu, R. Liu, K. Liu, Z. Sun, Q. Dai, *Nat. Commun.* **2016**, *7*, 12334.

[4] H. Hu, X. Yang, X. Guo, K. Khaliji, S. R. Biswas, F. J. Garcia de Abajo, T. Low, Z. Sun, Q. Dai, *Nat. Commun.* **2019**, *10*, 1131.

[5] X. Yang, F. Zhai, H. Hu, D. Hu, R. Liu, S. Zhang, M. Sun, Z. Sun, J. Chen, Q. Dai, *Adv. Mater.* **2016**, *28*, 2931.

[6] X. Yang, Z. Sun, T. Low, H. Hu, X. Guo, F. J. García de Abajo, P. Avouris, Q. Dai, *Adv. Mater.* **2018**, *30*, 1704896.

[7] J. Chen, M. Badioli, P. Alonso-González, S. Thongrattanasiri, F. Huth, J. Osmond, M. Spasenović, A. Centeno, A. Pesquera, P. Godignon, A. Zurutuza Elorza, N. Camara, F. J. G. de Abajo, R. Hillenbrand, F. H. L. Koppens, *Nature* **2012**, *487*, 77.

[8] Z. Fei, A. Rodin, G. Andreev, W. Bao, A. Mcleod, M. Wagner, L. Zhang, Z. Zhao, M. Thiemens, G. Dominguez, M. Fogler, A. Neto, C. Lau, F. Keilmann, D. Basov, *Nature* **2012**, *487*, 82.

[9] M. A. Huber, F. Mooshammer, M. Plankl, L. Viti, F. Sandner, L. Z. Kastner, T. Frank, J. Fabian, M. S. Vitiello, T. L. Cocker, R. Huber, *Nat. Nanotechnol.* **2017**, *12*, 207.

[10] Y. Abate, S. Gamage, Z. Li, V. Babicheva, M. H. Javani, H. Wang, S. B. Cronin, M. I. Stockman, *Light: Sci. Appl.* **2016**, *5*, e16162.

[11] S. Dai, Z. Fei, Q. Ma, A. S. Rodin, M. Wagner, A. S. McLeod, M. K. Liu, W. Gannett, W. Regan, K. Watanabe, T. Taniguchi, M. Thiemens, G. Dominguez, A. H. C. Neto, A. Zettl, F. Keilmann, P. Jarillo-Herrero, M. M. Fogler, D. N. Basov, *Science* **2014**, *343*, 1125.

[12] A. J. Giles, S. Dai, I. Vurgaftman, T. Hoffman, S. Liu, L. Lindsay, C. T. Ellis, N. Assefa, I. Chatzakis, T. L. Reinecke, J. G. Tischler, M. M. Fogler, J. H. Edgar, D. N. Basov, J. D. Caldwell, *Nat. Mater.* **2018**, *17*, 134.

[13] W. Ma, P. Alonso-Gonzalez, S. Li, A. Y. Nikitin, J. Yuan, J. Martin-Sanchez, I. Taboada-Gutierrez, I. Amenabar, P. Li, S. Velez, C. Tollan, Z. Dai, Y. Zhang, S. Sriram, K. Kalantar-Zadeh, S. T. Lee, R. Hillenbrand, Q. Bao, *Nature* **2018**, *562*, 557.

[14] F. Hu, Y. Luan, M. E. Scott, J. Yan, D. G. Mandrus, X. Xu, Z. Fei, *Nat. Photonics* **2017**, *11*, 356.

[15] Z. Fei, M. E. Scott, D. J. Gosztola, J. J. Foley, J. Yan, D. G. Mandrus, H. Wen, P. Zhou, D. W. Zhang, Y. Sun, J. R. Guest, S. K. Gray, W. Bao, G. P. Wiederrecht, X. Xu, *Phys. Rev. B* **2016**, *94*, 081402.

[16] J. Yuan, W. Ma, L. Zhang, Y. Lu, M. Zhao, H. Guo, J. Zhao, W. Yu, Y. Zhang, K. Zhang, H. Y. Hoh, X. Li, K. P. Loh, S. Li, C.-W. Qiu, Q. Bao, *ACS Photonics* **2017**, *4*, 3055.

[17] G. X. Ni, L. Wang, M. D. Goldflam, M. Wagner, Z. Fei, A. S. McLeod, M. K. Liu, F. Keilmann, B. Özyilmaz, A. H. Castro Neto, J. Hone, M. M. Fogler, D. N. Basov, *Nat. Photonics* **2016**, *10*, 244.

[18] A. Woessner, M. B. Lundeberg, Y. Gao, A. Principi, P. Alonso-Gonzalez, M. Carrega, K. Watanabe, T. Taniguchi, G. Vignale, M. Polini, J. Hone, R. Hillenbrand, F. H. Koppens, *Nat. Mater.* **2015**, *14*, 421.

**ADVANCED
SCIENCE NEWS**
www.advancedsciencenews.com

**ADVANCED
FUNCTIONAL
MATERIALS**
www.afm-journal.de

[19] P. Li, I. Dolado, F. J. Alfaro-Mozaz, F. Casanova, L. E. Hueso, S. Liu, J. H. Edgar, A. Y. Nikitin, S. Vélez, R. Hillenbrand, *Science* **2018**, *359*, 892.

[20] R. Hernandez, R. Juliano Martins, A. Agreda, M. Petit, J.-C. Weeber, A. Bouhelier, B. Cluzel, O. Demichel, *ACS Photonics* **2019**, *6*, 1500.

[21] A. Giugni, B. Torre, A. Toma, M. Francardi, M. Malerba, A. Alabastri, R. Proietti Zaccaria, M. I. Stockman, E. Di Fabrizio, *Nat. Nanotechnol.* **2013**, *8*, 845.

[22] A. Giugni, B. Torre, M. Allione, G. Das, Z. Wang, X. He, H. N. Alshareef, E. Di Fabrizio, *Adv. Opt. Mater.* **2017**, *5*, 1700195.

[23] O. Khatib, J. D. Wood, A. S. McLeod, M. D. Goldflam, M. Wagner, G. L. Damhorst, J. C. Koepke, G. P. Doidge, A. Rangarajan, R. Bashir, E. Pop, J. W. Lyding, M. H. Thiemens, F. Keilmann, D. N. Basov, *ACS Nano* **2015**, *9*, 7968.

[24] E. Yoxall, M. Schnell, A. Y. Nikitin, O. Txoperena, A. Woessner, M. B. Lundeberg, F. Casanova, L. E. Hueso, F. H. L. Koppens, R. Hillenbrand, *Nat. Photonics* **2015**, *9*, 674.

[25] S. Dai, Q. Ma, T. Andersen, A. S. McLeod, Z. Fei, M. K. Liu, M. Wagner, K. Watanabe, T. Taniguchi, M. Thiemens, F. Keilmann, P. Jarillo-Herrero, M. M. Fogler, D. N. Basov, *Nat. Commun.* **2015**, *6*, 6963.

[26] P. Li, M. Lewin, A. V. Kretinin, J. D. Caldwell, K. S. Novoselov, T. Taniguchi, K. Watanabe, F. Gaussmann, T. Taubner, *Nat. Commun.* **2015**, *6*, 7507.

[27] D. Hu, X. Yang, C. Li, R. Liu, Z. Yao, H. Hu, S. N. G. Corder, J. Chen, Z. Sun, M. Liu, Q. Dai, *Nat. Commun.* **2017**, *8*, 1471.

[28] A. Y. Nikitin, P. Alonso-González, S. Vélez, S. Mastel, A. Centeno, A. Pesquera, A. Zurutuza, F. Casanova, L. E. Hueso, F. H. L. Koppens, R. Hillenbrand, *Nat. Photonics* **2016**, *10*, 239.

[29] P. Alonso-González, A. Y. Nikitin, F. Golmar, A. Centeno, A. Pesquera, S. Vélez, J. Chen, G. Navickaite, F. Koppens, A. Zurutuza, F. Casanova, L. E. Hueso, R. Hillenbrand, *Science* **2014**, *344*, 1369.

[30] S. Dai, Q. Ma, Y. Yang, J. Rosenfeld, M. D. Goldflam, A. McLeod, Z. Sun, T. I. Andersen, Z. Fei, M. Liu, Y. Shao, K. Watanabe, T. Taniguchi, M. Thiemens, F. Keilmann, P. Jarillo-Herrero, M. M. Fogler, D. N. Basov, *Nano Lett.* **2017**, *17*, 5285.

[31] J. Duan, R. Chen, J. Li, K. Jin, Z. Sun, J. Chen, *Adv. Mater.* **2017**, *29*, 1702494.

[32] F. J. J. Clarke, D. J. Parry, *Light. Res. Technol.* **1985**, *17*, 1.

[33] M. Born, E. Wolf, *Principles of Optics: Electromagnetic Theory of Propagation, Interference and Diffraction of Light*, Elsevier, Amsterdam **2013**.

[34] A. Principi, M. Carrega, M. B. Lundeberg, A. Woessner, F. H. L. Koppens, G. Vignale, M. Polini, *Phys. Rev. B* **2014**, *90*, 165408.

[35] A. Principi, G. Vignale, M. Carrega, M. Polini, *Phys. Rev. B* **2013**, *88*, 121405.

[36] R. Courant, D. Hilbert, *Methods of Mathematical Physics: Partial Differential Equations*, Wiley, New York **2008**.

[37] A. Ambrosio, M. Tamagnone, K. Chaudhary, L. A. Jauregui, P. Kim, W. L. Wilson, F. Capasso, *Light: Sci. Appl.* **2018**, *7*, 27.

[38] K. Andersen, S. Latini, K. S. Thygesen, *Nano Lett.* **2015**, *15*, 4616.

[39] X. Guo, H. Hu, D. Hu, B. Liao, K. Chen, L. Liu, X. Zhu, X. Yang, Q. Dai, *Nanoscale* **2019**, *11*, 2703.

[40] A. Ciesielski, L. Skowronski, M. Trzcinski, E. Górecka, P. Trautman, T. Szoplik, *Surf. Sci.* **2018**, *674*, 73.

[41] S. Dai, M. Tymchenko, Y. Yang, Q. Ma, M. Pita-Vidal, K. Watanabe, T. Taniguchi, P. Jarillo-Herrero, M. M. Fogler, A. Alu, D. N. Basov, *Adv. Mater.* **2018**, *30*, 1706358.

[42] X. Guo, H. Hu, B. Liao, X. Zhu, X. Yang, Q. Dai, *Nanotechnology* **2018**, *29*, 184004.

[43] B. Zhao, Z. M. Zhang, *ACS Photonics* **2015**, *2*, 1611.

[44] B. Zhao, J. M. Zhao, Z. M. Zhang, *Appl. Phys. Lett.* **2014**, *105*, 031905.